Monatshefte für Chemie - Chemical Monthly (2020) 151:1715–1726
https://doi.org/10.1007/s00706-020-02696-1

ORIGINAL PAPER

Synthesis, structural investigations, DFT studies, and neurotrophic activity of zinc complex with a multidentate ligand

Mohammad Azam[1] · **Saikh Mohammad Wabaidur**[1,5] · **Saud I. Al-Resayes**[1] · **Mahboob Alam**[2] · **Md. Nazmul Haque**[3,4] · **Il Soo Moon**[4] · **Rajendra**[5]

Received: 24 April 2020 / Accepted: 23 September 2020 / Published online: 21 October 2020

Abstract

A novel zinc complex derived from a multidentate ligand, nitrilotris(ethane-2,1-diyl)tris(azanylylidene)tris(methanylylidene)-tris(2-methoxyphenol), was designed and structurally investigated by elemental analyses, IR, NMR, ESI-MS, and UV–Vis studies. The density functional theory was also recorded to investigate the additional insights into the structural and electronic properties of the ligand and its complex. Both the ligand and its complex showed significant neurite outgrowth and viability in brain neuron at lower concentration when investigated for neurological properties. Thus, it can be suggested that the ligand and its complex may play a potential role in brain development, functioning as well as in the treatment of neurological disorders.

Graphic abstract

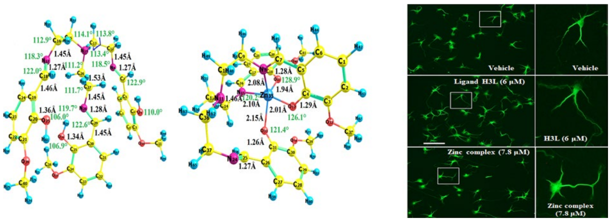

Keywords Zinc(II) complex · DFT studies · Neurotrophic activity

Introduction

Schiff base ligands, also known as privileged ligands, show a broad range of applications, particularly in food chemistry, organic synthesis, dyes and pigments, catalysis, and various biological applications [1–7]. The biological behaviour

---

Electronic supplementary material The online version of this article (https://doi.org/10.1007/s00706-020-02696-1) contains supplementary material, which is available to authorized users.

✉ Mohammad Azam
azam_res@yahoo.com; mhashim@ksu.edu.sa

✉ Mahboob Alam
mahboobchem@gmail.com

✉ Rajendra
krajendra@banasthali.in

[1] Department of Chemistry, College of Science, King Saud University, P. O. Box 2455, Riyadh 11451, Kingdom of Saudi Arabia

[2] Division of Chemistry and Biotechnology, Dongguk University, 123 Dongdae-ro, Gyeongju, Republic of Korea

[3] Department of Fisheries Biology and Genetics, Patuakali Science and Technology University, Patuakhali 8602, Bangladesh

[4] Department of Anatomy, School of Medicine, Dongguk University, Gyeongju 38066, Republic of Korea

[5] Department of Chemistry, Banasthali Vidyapith, Banasthali 304022, Rajasthan, India

exhibited by Schiff bases is supposed to be due to the presence of azomethine/imine linkage [8–10]. Over the years, the chemistry of Schiff bases has received extensive attention in coordination chemistry due to their ease in synthesis, denticity, strong chelating behaviour, flexible structures and, more importantly, in the formation of numerous coordination compounds with multiple applications in medicinal and material chemistry [11–20]. Literature reveals that the metal complexes with coordination number seven or higher are less developed [21, 22]. However, heptadentate Schiff base complexes, particularly tripodal complexes, constructed from tris(2-aminoethyl)amine are widely reported in literature due to their behaviour in encapsulating metal ions, and thus facilitating seven coordination geometry [23–27].

Alzheimer's disease (AD), the most common form of dementia, was first described by Alzheimer in 1906, and is the major public health concern with its increasing prevalence among elderly people [28–30]. The pathological hallmarks of AD include extracellular deposition of amyloid plaque and intraneuronal aggregation of neurofibrillary tangles, and are responsible for decrease in reserve capacity of the brain, which is determined by the number and neurite outgrowth of neurons [31–33]. A large number of evidences suggest that prevention of neurite damage by exogenous drugs can ameliorate the symptoms of neurological disorders such as AD by reconstructing the partially damaged neuronal network [34–36]. Over the last few years, there are several evidences to design the metal complexes intervening with the β-amyloid aggregation in a useful way to restore the metal homeostasis, essential for the diagnosis and therapeutics of Alzheimer's disease [37–41]. Considering the above facts, we are herein concerned in preparing a novel zinc complex obtained from tris(2-aminoethyl)amine-based tripodal ligand, and its application in intervening in β-amyloid aggregation, effective for diagnosis and therapeutics of AD. The tripodal Schiff ligand was prepared following the methods reported in literature [42, 43]. The synthesized complex was characterized by several physico-chemical techniques. Moreover, DFT calculation and time-dependent DFT (TD-DFT) were carried out to understand the geometry and electronic properties, including HOMO–LUMO analysis, molecular electrostatic potential (MEP), thermodynamic parameters, and global reactivity descriptors.

Results and discussion

The IR spectrum of free ligand H_3L revealed a characteristic band at 1634 cm^{-1} attributed to azomethine linkage. However, its position showed negative shift and appeared at 1630 cm^{-1} in complexation, suggesting the coordination of zinc ion via imine nitrogen (Fig. 1) [44–46]. Furthermore, bands at 736 cm^{-1}, 1041 cm^{-1} and 1041 cm^{-1} were assigned to aromatic ring vibrations of the ligand H_3L. However, no appreciable change was noticed in their position in the IR spectrum of zinc complex [44–46]. Besides, the IR spectrum of zinc complex exhibited a medium-intensity band at 3454 cm^{-1} attributed to $\upsilon_{(O–H)}$ vibrations [45–47]. Typical vibrational assignments of the zinc complex in the IR spectrum were also supported using the same B3LYP/6-311G(*d,p*) basis set applied in the optimization of complex geometry. From the calculated stretching vibration modes of the aromatic bands (C–H), CH_3, and $–CH_2–$ for the complex were found as a bundle of weak, including asymmetric and symmetrical intensities at 3225–3165 cm^{-1}, bundle of strong intensities at 3176–3007 and 3137–3039 cm^{-1} (unscaled), respectively (Fig. 1b). Other theoretically calculated important vibrations are at 3065 and 3031 cm^{-1} for *H*-C = N, 1730 cm^{-1} for H–C = N–, 1688–1670 cm^{-1} for Zn–N = C–, and 1110 cm^{-1} for –C–O– groups. However, all vibrations obtained using B3LYP/6-311G(*d,p*) basis set were measured in unscaled mode. The results revealed that the theoretical vibrations are almost correlated with the experimental data, and can be shown by comparing the spectra of ligand and zinc complex with the calculated complex spectrum.

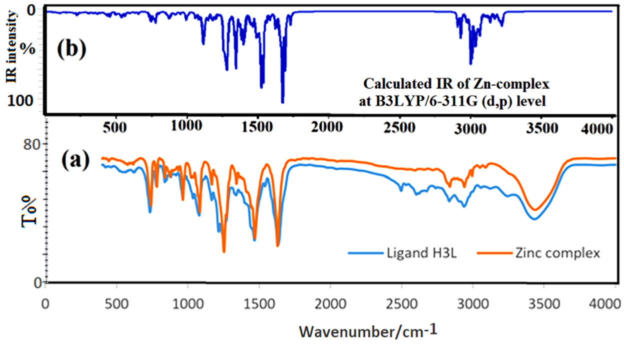

Fig. 1 IR spectra of ligand, H_3L, its zinc complex and calculated IR spectrum of the complex

The ^1H NMR spectrum of H_3L exhibited a characteristic sharp peak at 8.25 ppm assigned to azomethine proton (s, 3H, -**CH** = N-). Resonances due to $–OCH_3$ and phenyl protons appeared at 3.33 ppm and 6.53–6.97 ppm, respectively. Furthermore, proton resonances due to $–CH_2–N = $**CH**– appeared at 2.84 ppm, whereas –N–$\mathbf{CH_2}$– (s, 6H) exhibited proton resonance at 2.49 ppm. However, ^1H NMR spectrum of zinc complex revealed deshielding in chemical shifts, and showed a multiplet due to aromatic protons at 6.59–6.99 ppm (s, Ar–H, 9H), whereas the characteristic azomethine signal appeared at 8.27 ppm (s, 3H, -**CH** = N-). The chemical shifts due to $–OCH_3$ and methylene protons appeared at 3.37, 2.88 and 2.51 ppm, respectively.

^1H NMR spectral findings were further established by ^{13}C NMR spectra, revealing a characteristic azomethine carbon signal at 155.8 ppm in H_3L. Furthermore, ^{13}C NMR data exhibited –OCH_3 signal at 54.3 ppm, whereas the signals due to –N–CH_2–CH_2–N– appeared at 60.8 and 51.5 ppm, respectively. The position for ^{13}C NMR signals due to aromatic carbon appeared at 122.4–153.5 ppm. However, the ^{13}C NMR findings showed deshielding in complexation, suggesting the involvement of zinc ion in coordination.

The surface morphology of the complex, recorded at low magnification, exhibited beautiful morphology with spine-like randomly spread structures. The size of the particles varied and mainly existed in a few microns (Fig. 2). However, particles with size 100 µm were also observed, which agglomerated to form a large size.

TGA data revealed the degradation of the studied zinc complex in two distinct steps, exhibiting the first step at ca. 300 °C, equivalent to the loss of moisture constituting 2.94% of the total weight of the complex (Fig. 3). The complex degraded completely in the second and most important step at ca. 410 °C, revealing the loss of the whole organic moiety with 24.0% of the total weight of the complex, forming zinc oxide as the end product (9.49%).

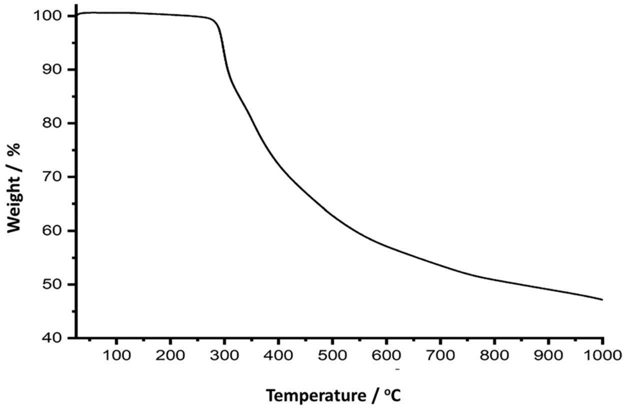

Fig. 3 TGA graph of zinc complex

Molecular geometry

Figure 4 shows the fully optimized geometry of the ligand, H_3L and the gas phase zinc complex using the basis set B3LYP/6-311(*d*,*p*) established in terms of energy with numbering of the atoms of complex used to calculate the bond strength and angles of the ligand and its complex. Figure 4a displays the coordination of zinc ion via azomethine, tertiary nitrogen and deprotonated hydroxyl oxygen. The designed zinc complex (Fig. 4b) shows its deformed geometry around the central metal ion. The bonds between carbon and nitrogen of azomethines extended slightly (Fig. 4) after complexation as compared to free ligand on account of the direct participation of nitrogen of azomethines in the formation of coordinated bonds with the zinc ion. Although the bond distance of phenolic oxygen (C–O) decreased marginally because of overlapping orbitals, it gained partial double bond character. The bond distances of C–O, N = H, N–Zn, and O–Zn calculated theoretically are nearly similar to the values reported for zinc complexes. The lengths of Zn–N at 2.10 and 2.08 Å, and the distances of Zn–O are within the range of 1.94–2.15 Å, consistent with the relevant literature data [48–50]. Due to the electron displacement of the ligand to the zinc ion, elongation in C = N–Zn bond lengths may take place (Fig. 4) [51–53]. After the coordination with zinc ion, the ligand lost its planarity, and angular deformation was noticed in zinc complex in the ligand fraction. The lengths of C7–N8, C10–N11, C16–N15, and C25–N24 bonds slightly elongated due to deformation. The C = N bond length extends in the free ligand from 1.276–1.285 to 1.295–1.301 Å in the complex, whereas the C10–N11 (sp3) bond lengths extend from 1.464 to 1.476 Å. But, the bond lengths for C18–O23, C4–O12, and C31–O33 are 1.288, 1.291, and 1.265 Å, respectively, in zinc complex. However, these values are shorter than the value calculated for the ligand at 1.361, 1.371, and 1.341 Å. A similar trend was observed for the other bond length in the zinc complex. A slight difference in the bond lengths contributes to the deviation of the bond angle from the normal

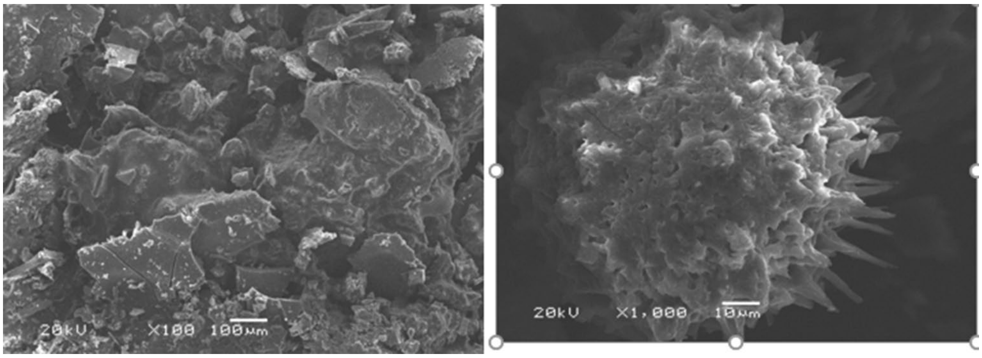

Fig. 2 SEM images of zinc complex

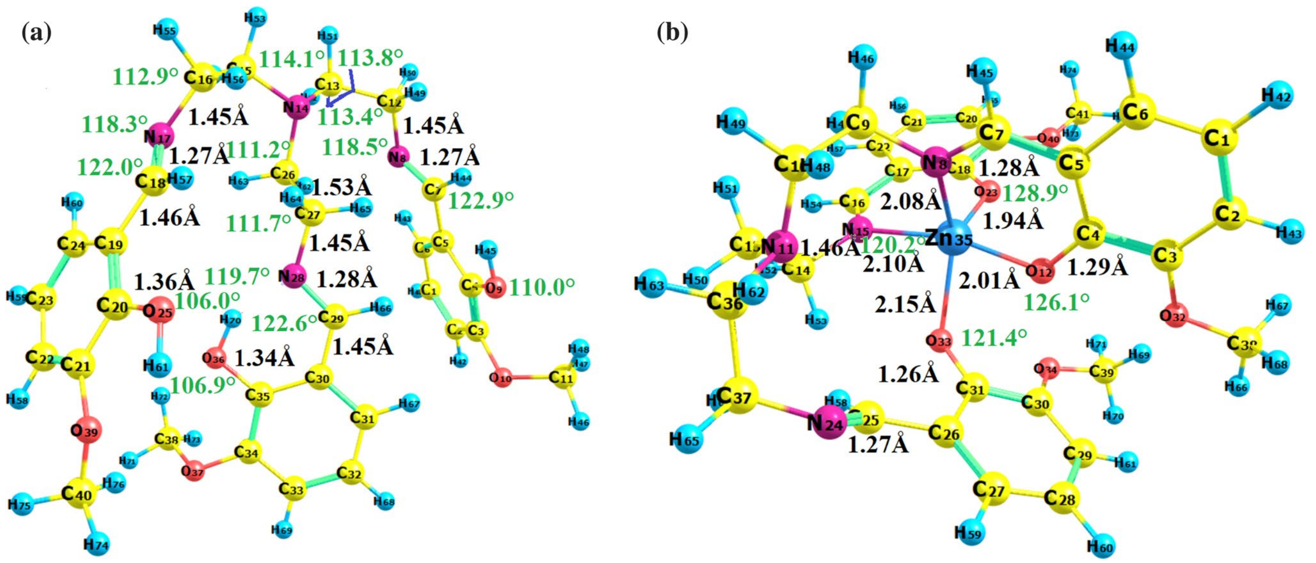

Fig. 4 Optimized structure of ligand (**a**) and its zinc complex (**b**) showing important bond lengths and angles in black and green, respectively (colour figure online)

value around the metal centre. The bond angles for zinc complex ∠O23Zn35N15, ∠O23Zn35012, ∠O12Zn35N8, ∠O23Zn35N8, ∠O23Zn35N11, and ∠O12Zn35N11 are 92.6°, 100.6°, 88.0°, 107.5°, 143.4°, and 110.4°, respectively. The complexation has no effect on the bond angle and length of benzene and other distantly residing groups. Selected geometry data of bond length and angles for ligand and complex are given in Table S1.

Electronic spectra of ligand and complex, frontier molecular orbitals, and molecular electrostatic potential (MEP)

The electronic spectra of H_3L and its zinc complex in ethanol (C_2H_5OH) are displayed in Fig. 5. However, the maximum absorption was observed at 345 nm due to the transformation of $n \rightarrow \pi^*$ before the complexation of the ligand [54–56].

However, its value shifted at 449 nm in the zinc complex. The LMCT interaction was driven by the coordination due to the extension of the larger conjugated system. The TD-DFT/B3LYP/6-311G(*d*,*p*) in ethanol determined the UV–Vis spectra of the ligand and its zinc complex. The calculated and experimental data for the UV–Vis spectra are given in Table S2. GaussSum2.2 was used to calculate and prepare group contributions of molecular orbit and UV–Vis spectra, respectively. UV–Vis spectra obtained from TD-DFT/B3LYP/6-311G(*d*,*p*) can be seen to be logically related to the experimental data. However, deviations from the experimental data were due to the influence of solvent, causing the change in the geometric and electronic structure, such as the molecular properties, and thus lower the energy of the molecules. In addition, solvent effect creates larger bands of absorption [57]. Frontier molecular orbitals (FMOs) play an important role in understanding the chemical behaviour of the complexes using the highest occupied molecular orbital (HOMO) and lower unoccupied molecular orbital (LUMO) associated with electronic transition. Table S2 clearly states that the transitions at 490 and 348 correspond to beta spin HOMO–LUMO and alpha spin HOMO–LUMO with transition contributions of 55 and 52, respectively. On the other hand, peaks at 327 and 326 nm induce β-spin HOMO–LUMO and α-spin HOMO–LUMO in the electronic transition with 70% and 74% contributions. However, the major transitions observed in the theoretical UV–Vis spectrum at 331, 321, and 318 nm correspond to various HOMO–LUMO energy levels with a spectrum transition contribution of 61, 83, and 89% in the free ligand. Certain bands observed at 264 and 251 with transitional contributions of 94 and 93% appear because of $\pi \rightarrow \pi^*$ transition.

Cluster continuum model (CCM) [58] was applied to test the solvent effect directly on the electronic transition of the zinc complex by supplying ethanol molecule to the adjacent complex at the appropriate place, and using the same level theory. Ethanol solvent was considered as explicit EtOH in the cluster continuum approach and the result obtained from the calculation indicated that explicit ethanol molecule was not involved in the HOMO–LUMO system as shown in Fig. 6. Therefore, there was no significant contribution to the electronic transition and, consequently, no apparent effect of the explicit ethanol on the UV–Vis spectrum of metal complex was observed in contrast to the implicit solvent in the system (Fig. 5). Theoretical UV–Vis spectrum of the zinc complex calculated in the presence of explicit solvent in the

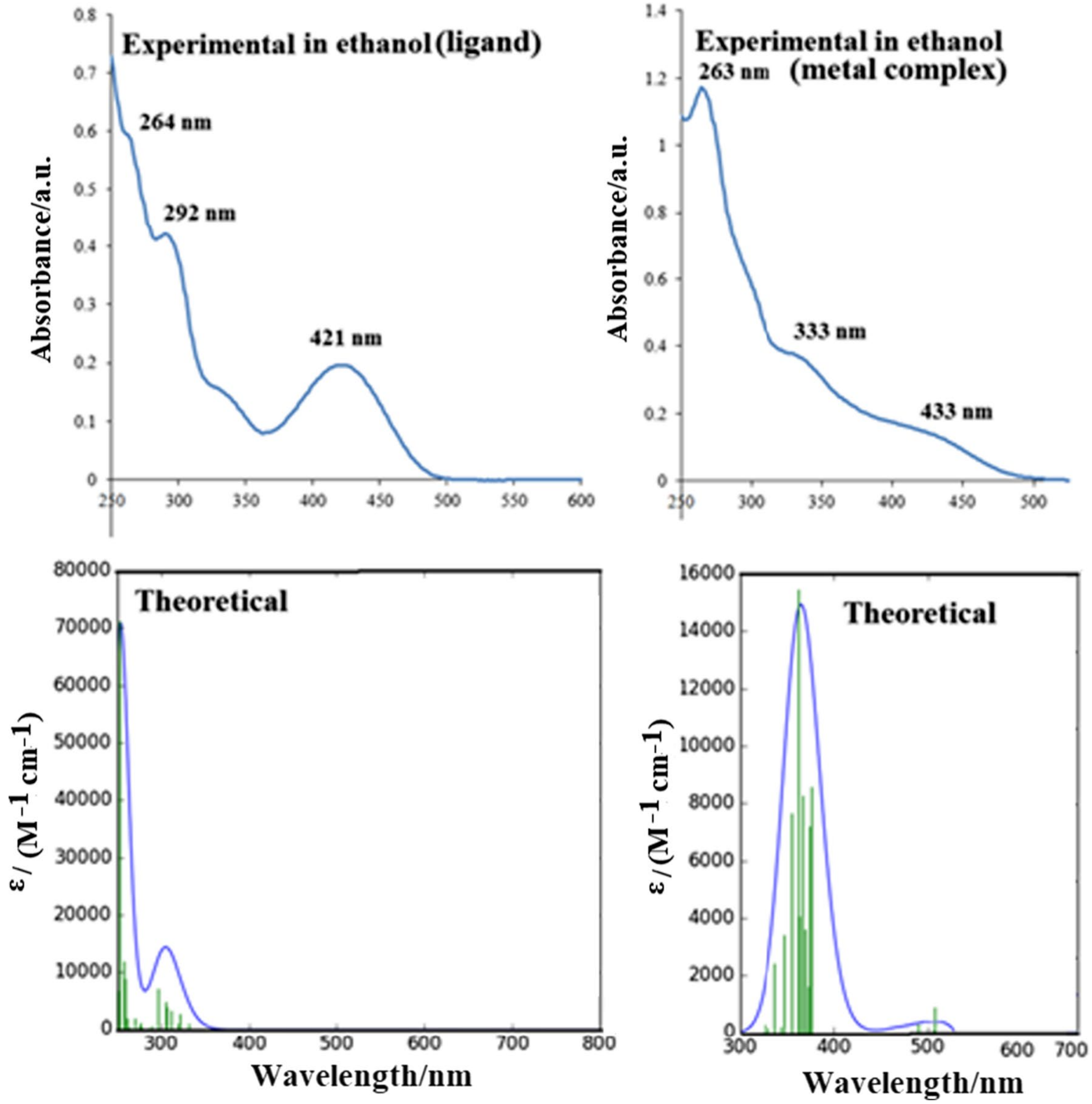

Fig. 5 The comparison of experimental and calculated UV–Vis spectra of the ligand and zinc complex in ethanol

system was found to be almost the same as in the presence of implicit ethanol solvent in the system.

The molecular geometry selected for the complex calculations has doublet multiplicity. Therefore, the frontier molecular orbitals called higher occupied molecular orbitals (HOMO) and lower unoccupied molecular orbitals (LUMO) are divided into molecular orbitals alpha (spin ↑) and beta (spin ↓). The metal complex isodensity plots along with the energy values of the frontier orbitals are shown in Fig. 6. The basic electronic properties of any molecule are mostly based on HOMO–LUMO molecular orbitals and band gaps. From Fig. 7 of the zinc complex, the FMO$_S$ of alpha and beta energies are $E_{\mathrm{HOMO}} = -5.06$ eV (α), $E_{\mathrm{HOMO}} = -5.05$ eV (β), $E_{\mathrm{LUMO}} = -1.25$ eV, and $E_{\mathrm{LUMO}} = -3.78$ eV and their corresponding energies gaps are ($\Delta E = E_{\mathrm{LUMO}} - E_{\mathrm{HOMO}}$) are 3.81 (α-spin), 1.27 eV (β-spin). The energy gap of the zinc complex ($\Delta E = 3.81$ and 1.27 eV) is lower in comparison to the energy gap of ligand ($\Delta E = E_{\mathrm{LUMO}} - E_{\mathrm{HOMO}} = -1.39 - 5.39 = 4.0$ eV, Fig. S1), suggesting that the Zn(II) ion has a greater propensity to accept electrons from phenolic oxygen and azomethine nitrogen to enter in the complex formation. The molecular orbital energies (E_{HOMO} and E_{LUMO}) calculated by applying B3LYP/6-311G(*d*,*p*) level theory are found to be all negative, suggesting that both the ligand and its zinc complex are stable [59, 60]. The energy contribution of these orbits shows the capacity of quantitative chemical reactions, such as chemical potential, electrophilicity, chemical hardness, and softness. The small gap

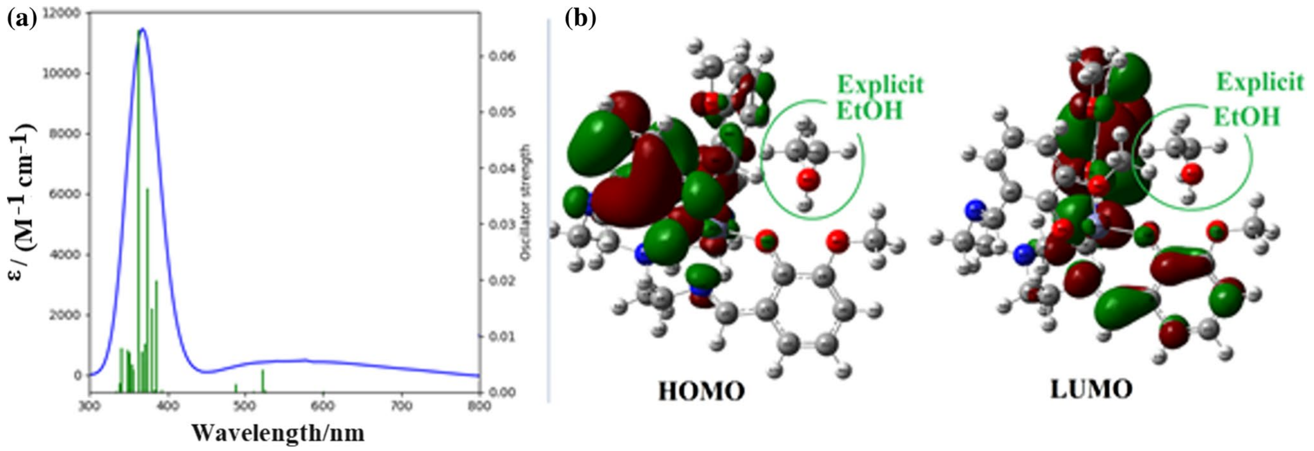

Fig. 6 **a** Theoretical UV spectrum of the zinc complex, and **b** HOMO–LUMO molecular orbital graphs in the presence of explicit ethanol

Fig. 7 The HOMO and LUMO of Zn complex and its energy gaps

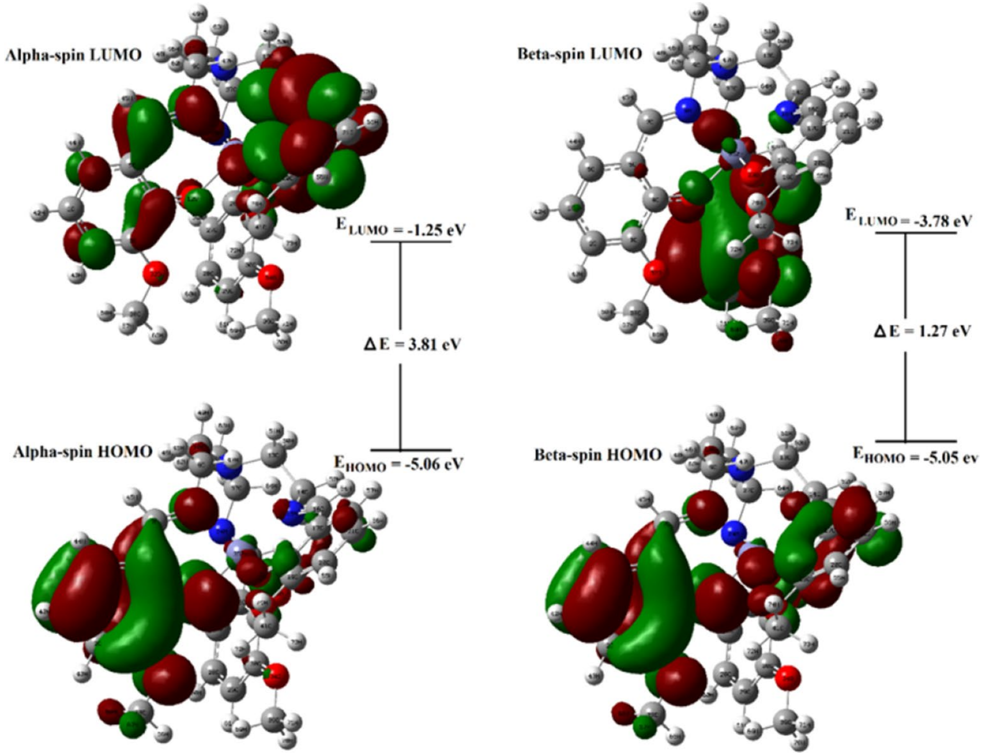

between HOMO and LUMO gives an indication about the high chemical reactivity and the low kinetic stability of the complex. HOMO and LUMO are located on one of the three aromatic fragments of the complex for α (spin ↑), whereas HOMO is distributed on two of the three aromatic skeletons of the complex, and LUMO is primarily on one of the three aromatic rings for β (spin ↓) (Fig. 6). The SCF energy, dipole moment, frontier molecular orbitals energy eigenvalues and its energy gap, and global chemical reactivity indices are calculated using B3LYP/6-311G(*d*,*p*) basis set as shown in Table S3.

The molecular electrostatic potential (MEP) map of the ligand and its zinc complex is measured and used to analyse the binding properties. In addition to determining the presence of inter- or intramolecular interactions in the ligand and its complex, MEP map may be used to determine the reactivity of the molecules. In these MEP diagrams, the different colours were related to the electrostatic potential of the surface molecules. Most ligand surfaces are neutral by showing green on it with the exception of some areas where yellow colour is observed, suggesting a slight negative potential. Activation of such areas need stimulus to intensify the reaction by supplying extra energy, either stirring, refluxing or both. The MEP ligand diagram (Fig. 8a) shows the richness in electron density due to the presence of ligand nitrogen (–C = N) and phenolic groups (C–O), participating in bonding with Zn(II) ion. In this process, the redistribution of the electron density between the ligand and zinc ion provides the formation of new bonds, such as coordination and covalent bonds, resulting in new lengths and angles of metal complexes that have a direct effect on the MEP electron density of the metal complex. Figure 8b displays the MEP surface and contour plot with colour ranging from darkest red to deepest blue. Most of the regions in the complex are neutral and shown in green colour. The negative electrostatic potential is observed on oxygen atoms as shown by the slight red colour [61, 62] (Fig. 8b). The dominance and electron deficiency in specific regions define the variability of the high to low electrostatic potential. The maximum positive and negative potential region of molecular electrostatic potential map on the complex being studied is the preferred site in the chemical system for nucleophilic and electrophilic attacks.

Thermodynamic parameters and global reactivity descriptors

Thermodynamic parameters, dipole moment, and descriptors of chemical reactivity are important molecular properties on the basis of HOMO–LUMO and its energy gap [63]. The parameters mentioned above were calculated using the theory level B3LYP/6-311G(*d*,*p*). However, to study the thermodynamic properties of molecules, DFT methods are important tools. The accuracy of the thermodynamics parameters are based on the perfect geometry as well as vibrational data. Thermodynamic data such as thermal energy, molar heat capacity and entropy of the complex are given in Table S3. The total dipole moments of any chemical compound associated with the neighbourhood interaction are used to explain the nature and strength of the interaction with the surrounding environment. The present complex with the dipolar moment 2.29 D presents an intermediate interaction with the neighbouring environment and indicates the degree of delocalization of the charges, hardness, chemical potential, electrophilicity index, electronegativity, ionization potential and softness under category of global reactivity descriptors are shown in Table S1. Global reactivity descriptors are applied to evaluate the properties of a complex. The global reactivity descriptors define a compound reactivity as well as kinetic stability relying on FMOs. It is worth mentioning that molecules with a large molecular orbital gap or high chemical hardness values are commonly called hard molecules with less polarizability, high kinetic stability, and low chemical reactivity. Significance of energy gaps has been described under the section of electronic spectra of ligand and complex. The concept of hardness (η) is associated with the reactivity of a compound which counts the degree of chemical reactivity to which the addition of a charge stabilizes the system. A molecule with a higher softness value ($S = 0.524$ eV) (ES) (low η value; Zn complex; $\eta = 1.95$ eV) indicates the stabilization of charge than a molecule with a smaller S (ligand; $S = 0.5$ eV) value (high η value, ligand; $\eta = 2$ eV). The ionization potential and the electronic affinity are extracted from the values of

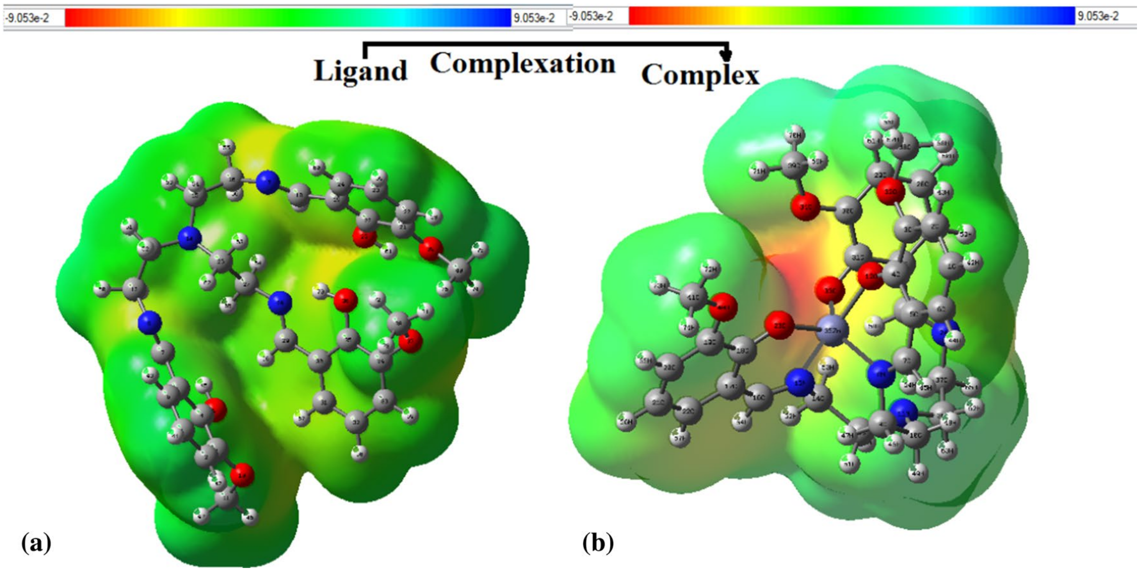

Fig. 8 Molecular electrostatic potential (MEP) surface of the studied ligand (**a**) zinc complex (**b**) showing red colour reflects the highest negative area favourable for electrophilic attack (colour figure online)

the energies HOMO and LUMO as $I = -E_{\mathrm{HOMO}}$ and $A = -E_{\mathrm{LUMO}}$. Furthermore, a large energy gap HOMO–LUMO signals a hard molecule and relates to more stable molecules, whereas a small energy gap specifies a soft molecule and relates to a more reactive molecule. The electrophilicity index (ω) has been applied for chemical reactivity of complex and ligand to test the ability of a chemical compound to accept an electron from its reaction partner. A reactive species acting as a nucleophile is described as having a lower value of ω. The lower electrophilicity index of ligand ($\omega = 2.87$ eV) (Table S3) than that of $ZnCl_2$ ($\omega = 6.10$ eV) indicates the donation of the ligand electron to Zn(II) ion to form the complex.

Concentration, optimization, and differential neurite outgrowth promoting the activity of the ligand and zinc complex

To investigate the neurotrophic factor-mimetic property of the tested compounds, we cultured E19 rat hippocampal neurons, and incubated for 3 days in the presence of ligand and its zinc complex for the analysis of morphometric parameters, i.e. the primary neurite number (neurites that originated directly from soma), total length of primary neurites (TLPN; sum of the length of primary neurites) and the longest length of primary neurites (LLPN). In a preliminary experiment, the ligand and its zinc complex were added in different concentrations and their neuritogenic activities (Fig. 9A) were measured according to the method described by Hannan et al. [64, 65]. We found that the ligand exhibited the highest activity at 6 nM concentration based on primary neurite (PNN; increase by ~ 8% of vehicle; $P > 0.05$) counts (Fig. 9B-a), total lengths of PNs (TLPN; increase by ~ 30% of vehicle; $P < 0.05$) (Fig. 9B-b) and lengths of longest primary neurites (LLPNs; increase by ~ 45% of vehicle; $P < 0.05$) (Fig. 9B-c) compared to the vehicle control [DMSO, final concentration < 1.0% (*v*/*v*)], and these neuritogenic activities consecutively decrease with increase in the concentration of H_3L, i.e. 1.8 µM, 3.6 µM, and 7.2 µM. However, in case of the zinc complex, neuritogenic activities increase initially, i.e. evidenced by the enhancement of TLPN (increase by ~ 12% of vehicle; $P > 0.05$) ([Fig. 9B---e) and LLPN (increase by ~ 10% of vehicle; $P > 0.05$) (Fig. 9B---f), but not PNN (Fig. 9B---d) at 2.6 nM concentration and this activity reaches maximum at 7.8 nM concentration, i.e. PNN (increase by ~ 5% of vehicle; $P > 0.05$; and > ~ 30% of 2.6 nM PNN), TLPN (increase by ~ 15% of vehicle; $P > 0.05$; and > ~ 3% of 2.6 nM TLPN), LLPN (increase by ~ 33% of vehicle; $P < 0.05$; and > ~ 23% of 2.6 nM LLPN) and then decrease with increase in the concentration of the complex, i.e. 1.6 µM and 3.2 µM. In addition, viability analysis using trypan blue exclusion assay at DIV6 revealed that both the ligand (6 µM) and zinc complex (7.8 µM) protected cultured neurons from naturally occurring cell death as compared to vehicle and notably the zinc complex showed higher neuronal protection over the ligand by ~ 3% (Fig. 9C).

The morphological development of neuron is characterized by highly organized, stereotyped process that comprised neurite outgrowth, followed by axonal sprouting, dendritic remodelling, and maturation by the formation of synapses through special dendritic features called spines. Neurons grow specialized cell protrusions known as neurites that are the core for structural and functional polarity [66] and form the basis of establishment of synaptic connections during development [67], thus playing a fundamental role in the formation of highly interconnected neuronal networks in the brain [68, 69]. In neurodegenerative brains, the neural networks are disrupted due to the regression of neurites and subsequent neuronal death [34]. In such conditions, exogenous drugs of natural or synthetic origin, known to support neuronal networks by extending axonal and dendritic arbors in developing neurons and restore partially damaged network in degenerating brain, could ideally be a curative means [70]. The present study shows that ligand, H_3L and zinc complex can modify neuronal survival and cytoarchitecture by neuronal sprouting, which would ultimately promote the extent of neuronal networks and may help in reconstruction of the damaged brain in neurodegenerative diseases such as Alzheimer's.

The result represents fthe luorescence photomicrograph of hippocampal cultures after treatment of different compounds with their highest neuritogeneic activity, that is, PNN, TLPN and LLPN for 3 days (Fig. 9A, Ba–f). Assessment was made of neuronal viability at DIV6 after trypan blue exclusion, and arrow indicates dead cells (Fig. 9C). Scale bar 40 µM. Bars represent means ± SEM ($n = 30$ individual neurons). Statistically significant vs. vehicle: $^{*}P < 0.05$, $^{**}P < 0.01$, and $^{***}P < 0.001$ (ANOVA).

Conclusions

A novel zinc complex possessing tripodal ligand was synthesized and characterized by several methods. DFT analyses were conducted to calculate the geometric parameters, transition patterns and FMOs to know the nature of the interaction of the ligand with Zn(II) ion. Both the ligand and its zinc complex were investigated by cell biological assay and exhibited neuronal outgrowth by PNN (~ 5%), TLPN (~ 15%), and LLPN (~ 30%) and survival-promoting activities in the primary culture of hippocampal neuron at lower concentration, suggesting a therapeutic promise in the development of a drug for the treatment of neurological disorders.

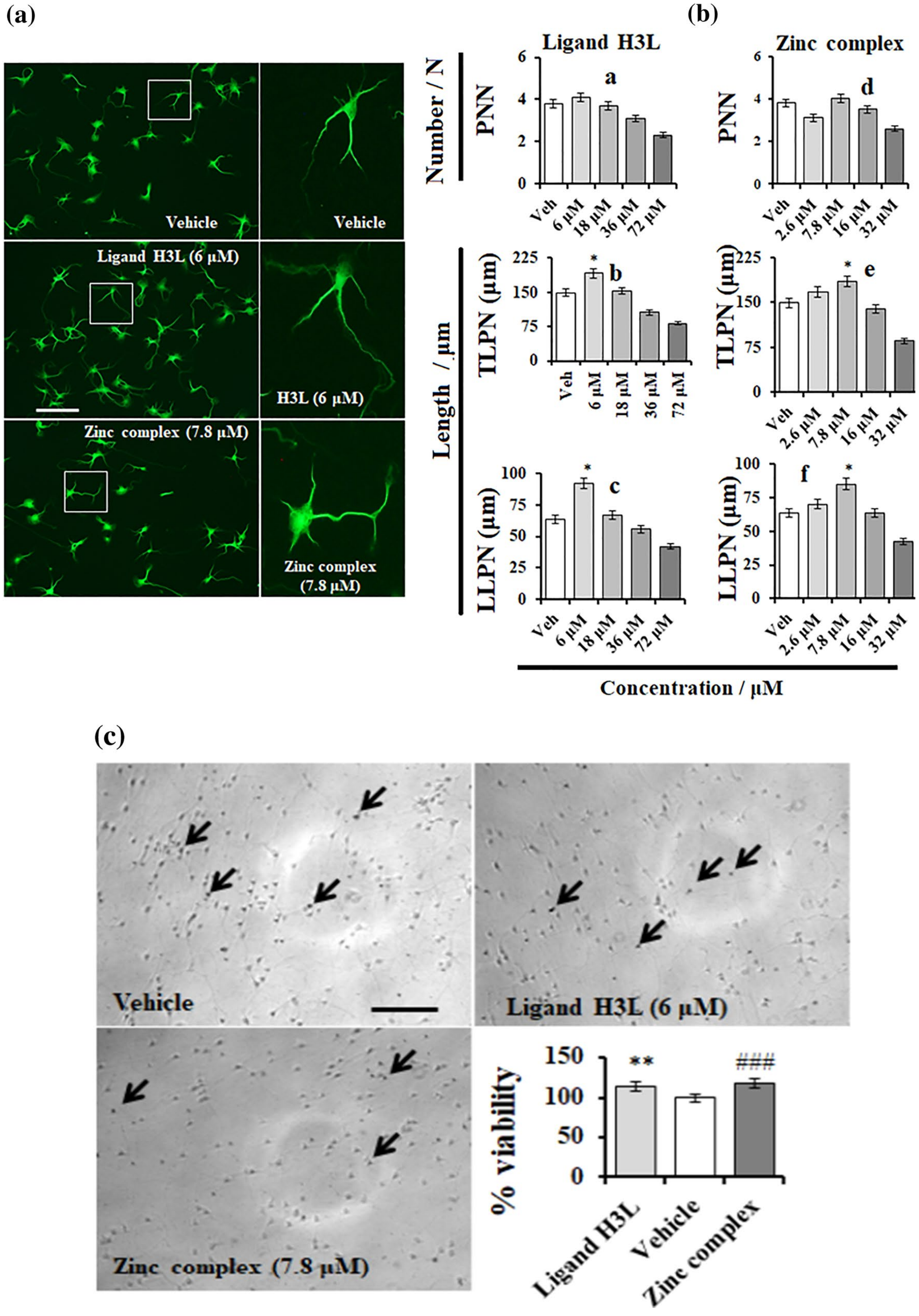

Fig. 9 Evaluation of the neuritogenic activities and neuronal viability of synthesized H_3L and its zinc complex

Experimental

C, H, N data were obtained using ElementarVarrio EL analyzer. The electronic spectra were obtained from LKB Biochem UV–visible spectrophotometer at room temperature in ethanol. FT-IR spectra were collected from Perkin Elmer 621 spectrophotometer at 4000–400 $\mathrm{cm^{-1}}$. SDTQ-600 (TA) was used to study the thermal analyses of the complex in inert atmosphere. SEM images were obtained from JSM-6380 LA with a magnification value of X 18 TO 300,000 at resolution 3.0 nm (30 kV, WD8MM, SEI) and voltage of 30 kV at JSM-6380 LA.

Gaussian's WebMo platform [71, 72] was used to conduct the entire computation of H_3L and its zinc complex. The ligand and its complex geometry optimization were established using unrestricted B3LYP with 6-311G(*d*,*p*) level set in gas and solvent (C_2H_5OH, $\varepsilon = 24.852$, $\mu = 1.69$, and $n_D = 1.3611$) [73, 74]. Harmonic vibrational frequency analyses were tested to know the imaginary frequency to ensure the reliability of the optimized structure, showing the true minimum on the potential energy field with no imaginary frequency. The HOMO–LUMO gap in C_2H_5OH solution was also analysed using the excitation energy of HOMO–LUMO obtained by TD-B3LYP/6-311G(*d*,*p*) calculation and termed as the polarizable continuum model (PCM) [75, 76]. The zinc complex with reactive sites was visualized via the surface of the electrostatic molecular potential (MEP). The MEP was rendered using the GaussView 5 program to map the electrostatic potential to the total electron density of the molecule [77, 78]. In addition, various physical parameters and descriptors were calculated to know the behaviour of the present molecule.

Nitrilotris(ethane-2,1-diyl)tris(azanylylidene)-tris(methanylylidene)tris(2-methoxyphenol) (H_3L, $C_{30}H_{36}N_4O_6$) A methanol solution of tris(2-aminoethyl) amine was added to the solution of *o*-vanilin in 1:3 stoichiometric ratio in the same solvent. The reaction mixture was stirred for 12 h at room temperature, which was then evaporated to yield yellow coloured microcrystalline product in a week (Scheme 1). Yield: 82%; ESI-MS: $m/z = 550.26$ (M^+); ^{1}H NMR (400 MHz, DMSO-d_6): $\delta = 8.22$(s, –**C**H=N, 3H), 6.56–6.94 (*m*, 9H, **H**–Ar), 3.71 (s, 9H, –OC**H**$_3$), 1.93 (–C**H**$_2$–), 1.89 (–C**H$_2$**–) ppm; ^{13}C NMR (100 MHz, DMSO-d_6): $\delta = 166.9$ (–**C**H=N), 153.2 (Ar–**C1**–OH), 148.7 (–Ar–**C2**–O–CH$_3$), 123.7 (Ar–**C1**), 121.3 (Ar–**C6**), 117.8 (Ar–**C4**), 115.0 (Ar–**C3**), 56.6 (–CH$_2$–CH$_2$–), 56.2 (—CH$_2$–CH$_2$–), 55.4 (–O–CH$_3$) ppm; IR (KBr): $\bar{\nu} = 1645\ \upsilon_{(CH=N)}\ \mathrm{cm^{-1}}$.

Scheme 1

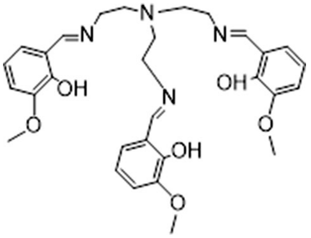

[Tris(salicylaldenimino)ethylamine]zinc(II) ($C_{30}H_{33}N_4O_6Zn$) To the solution of ligand H_3L in methanol, hydrated zinc chloride and NH_4PF_6 were added. The reaction mixture was refluxed for 10 h and then allowed to cool at room temperature, followed by the concentration of the reaction mixture under reduced pressure. The product was washed with water and re-crystalized in methanol. A crystalline product was formed upon slow evaporation of the solvent. However, no crystal was found suitable for single crystal X-ray diffraction. Yield: 62%; ESI-MS: $m/z = 610.17$ (M^+); ^{1}H NMR (400 MHz, DMSO-d_6): $\delta = 8.21$ (*s*, 3H, –**C**H=N), 6.56–7.10 (*m*, 9H, Ar–**H**), 3.85 (*s*, 9H, –O–C**H**$_3$), 2.87 (–CH$_2$), 2.79 (–CH$_2$) ppm; ^{13}C NMR (100 MHz, DMSO-d_6): $\delta = 170.5$ (–**C**H=N–), 159.3 (Ar–CH=N-) 157.5 (Ar–**C1**–O–), 136.6 (Ar–**C2**–O–CH$_3$), 121.1 (Ar–**C5**–), 120.1 (Ar–**C4**–)-120.4 (Ar–**C6**-), 117.1 (Ar–**C3**-) 55.1 (–O–**C**H$_3$), 54.4 (–N–**C**H$_2$–CH$_2$–N=), 50.2 (–N–CH$_2$–**C**H$_2$–N=) ppm; IR (KBr): $\bar{\nu} = 1625\ \upsilon_{(CH=N)}\ \mathrm{cm^{-1}}$.

Cell culture and extract treatment

All experimental procedures were performed in accordance with institutionally approved protocols specified by the Dongguk University Animal Care and Use Committee (approval certificate number IACUC-2015–002). Primary hippocampal neurons were prepared from Sprague–Dawley rat of embryonic day 19 (E19) pups' brain. Briefly, a pregnant rat was anaesthetized with isoflurane and foetal hippocampi were dissected; tissue dissociation and neuronal culture were carried out as described [64, 65]. In serum-free neurobasal medium supplemented with b27, cultures were maintained at 37 °C in a 5% CO_2/95% air atmosphere condition. The complex or vehicle [DMSO, final concentration < 1.0% (*v*/*v*)] were added to media prior to cell plating. All chemicals used in cell cultures were procured from Invitrogen (Carlsbad, CA), unless otherwise stated.

Immunofluorescence microscopy

After sequential paraformaldehyde/methanol fixation [79], neurons were treated with neuron-specific mouse monoclonal microtubule-associated protein 2 (MAP2; 1:500, Sigma, St. Louis, MO), primary antibody, followed by secondary antibody-tagged with Alexa fluor 488-conjugated goat anti-mouse IgG [1:1000, Molecular Probes, Eugene, OR]. Images were developed by Leica DM IRE2 microscope (Leica Microsystems AG, Wetzlar, Germany) equipped with high-resolution CCD camera (CoolSNAP™; Photometrics Inc., Tucson, AZ) using Leica FW4000 software and then processed through Adobe Photoshop 7.0 (San Jose, CA). Morphometric analysis and quantifications minimum of 30 cells were performed as described previously [64, 65] using Image J software (version 1.45) plug-in with simple neurite tracer (National Institute of Health, Bethesda, MD).

Statistical analysis

Results were presented as the means ± SEM of three independent experiments. Statistical analyses were conducted using ANOVA in SPSS version 17.0 (SPSS Inc., Chicago, IL). P values of $^{*}P<0.05$, $^{**}P<0.01$, and $^{***}P<0.001$, were considered statistically significant throughout.

Acknowledgements The authors acknowledge the financial support through Researchers Supporting Project number (RSP-2020/147), King Saud University, Riyadh, Saudi Arabia.

References

1. Ye X, Chen Y, Ling C, Ding R, Wang X, Zhang X, Chen S (2018) Dalton Trans 47:10915
2. Ding SY, Gao J, Wang Q, Zhang Y, Song WG, Su CY, Wang W (2011) J Am Chem Soc 133:19816
3. Demitri C, Maria BV, Madaghiele M, Corcione CE, Maffezzoli A (2016) Measurements 90:418
4. Liu Y, Mao L, Yang S, Liu M, Huang H, Wen Y, Deng F, Li Y, Zhang X, Wei Y (2018) Dyes Pigm 158:79
5. Wahba OAG, Hassan AM, Naser AM, Mohy-Eldin Gabr A (2017) Pigment Resin Technol 46:286
6. Sztanke K, Maziarka A, Osinka A, Sztanke M (2013) Bioorg Med Chem 21:3648
7. Abdel-Rahman LH, Abu-Dief AM, Aboelez MO, Hassan Abdel-Mawgoud AA (2017) J Photochem Photobiol B 170:271
8. Azam M, Al-Resayes SI, Kruszynska AT, Kruszynski R, Shakeel F, Soliman SM, Alam M, Khan MR, Wabaidur SM (2020) J Mol Struct 120:127177
9. Bringmann G, Dreyer M, Faber JH, Dalsgaard PW, Staerk D, Jaroszewski JW, Ndangalasi H, Mbago F, Brun R, Christensen SB (2004) J Nat Prod 67:743
10. Guo Z, Xing R, Liu S, Zhong Z, Ji X, Wang L, Li P (2007) Carbohydr Res 342:1329
11. Sacconi L, Bertisi I, Morassi R (1967) Inorg Chem 6:1548
12. Bhattacharya P, Parr J, Ross AT, Slawin AMZ (1998) J Chem Soc Dalton Trans. https://doi.org/10.1039/a806058d
13. Basak S, Sen S, Banerjee S, Mitra S, Rosair G, Rodriguez MTG (2007) Polyhedron 26:5104
14. Biswas C, Drew MGB, Ruiz E, Estrader M, Diaz C, Ghosh A (2010) Dalton Trans 39:7474
15. Kaczmarek MT, Zabiszak M, Nowak M, Jastrzab R (2018) Coord Chem Rev 370:42
16. Xin Y, Yuan J (2012) Polym Chem 3:3045
17. El-Bindary AA, El-Sonbati AZ, Diab MA, Ghoneim MM, Serag LS (2016) J Mol Liq 216:318
18. Al Zoubi W, Al Mohanna N (2014) Spectrochim Acta A 132:854
19. Jeevadason AW, Murugavel KK, Neelakantan MA (2014) Renew Sustain Energy Rev 36:220
20. Zhang J, Xu L, Wong WY (2018) Coord Chem Rev 355:180
21. Liu X, Hamon JR (2019) Coord Chem Rev 389:94
22. Yang LW, Liu S, Wong E, Rettig SJ, Orvig C (1995) Inorg Chem 34:2164
23. Keypour H, Salehzadeh S, Pritchard RG, Parish RV (2000) Polyhedron 19:1633
24. Zhang Y, Bhadbhade M, Kong L, Karatchevtseva I, Zheng R (2017) Polyhedron 138:82
25. Golbedaghi R, Moradi S, Salehzadeh S, Blackman AG (2016) J Mol Struct 1108:727
26. Bernhardt PV, Flanagan BM, Riley MJ (2000) Aust J Chem 53:229
27. Lamesato M, Nagahara K, Igarshi K, Sato KI, Kikkawa Y, Goto M (2011) Inorg Chim Acta 367:225
28. Alzheimer A, Stelzmann R, Schnitzlein HN, Murtagh FR (1995) Clin Anat 8:429
29. Ferri CP, Prince M, Brayne C, Brodaty H, Fratiglioni L, Ganguli M, Hall K, Hasegawa K, Hendrie H, Huang Y, Jorm A, Mathers C, Menezes PR, Rimmer E, Scazufca M (2005) Lancet 366:2112
30. Middleton LE, Yaffe K (2009) Arch Neurol 66:1210
31. Mayeux R (2003) Annu Rev Neurosci 26:81
32. Mortimer JA, Snowdon DA, Markesbery WR (2003) J Clin Exp Neuropsychol 25:671
33. Hou Y, Dan X, Babbar M, Wei Y, Hasselbalch SG, Croteau DL, Bohr VA (2019) Nat Rev Neurol 15:565
34. Galvan V, Bredesen DE (2007) CNS Neurol Disord Drug Targets 6:303
35. Chuang TT (2010) Biochim Biophys Acta 1802:872
36. Schaeffer EL, Novaes BA, da Silva ER, Skaf HD, Mendes-Neto AG (2009) Prog Neuropsychopharmacol Biol Psychiatry 33:1087
37. Kenche VB, Hung LW, Perez K (2013) Angew Chem Int Ed 52:3374
38. Collin F, Sasaki I, Eury H, Faller P, Hureau C (2013) Chem Commun 49:2130
39. Lim S, Paterson BM, Fodero-Tavoletti MT (2010) Chem Commun 46:5437
40. Greenough MA, Camakaris J, Bush AI (2013) Neurochem Int 62:540
41. Faller P, Hureau C (2012) Coord Chem Rev 256:2127
42. Costes JP, Dupuis A, Commenges G, Lagrave S, Laurent JP (1999) Inorg Chim Acta 285:49
43. Costes JP, Dahan F, Dupuis A, Lagrave S, Laurent JP (1998) Inorg Chem 37:153
44. Al-Resayes SI, Shakir M, Shahid N, Azam M, Khan AU (2016) Arab J Chem 9:335
45. Azam M, AlResayes SI (2016) J Mol Struct 1107:77
46. Nakamoto K (1970) Infrared spectra of inorganic and coordination compounds. Wiley Interscience, New York
47. Azam M, Wabaidur SM, Alam MJ, Kruszynska AT, Kruszynski R, Alam M, Al-Resayes SI, Dwivedi S, Khan MR, Islam MS, Albaqami NTM (2019) Inorg Chim Acta 487:97
48. Li X, Yu Z, Guan T, Li X, Ma G, Guo X (2014) Cryst Growth Des 15:278
49. Wang T, Zhu R-R, Zhang X-F, Yan T, Wang Q, Feng J, Zhou J, Du L, Zhao Q-H (2018) RSC Adv 8:7428
50. Li X, Cao R, Sun D, Bi W, Wang Y, Li X, Hong M (2004) Cryst Growth Des 4:775
51. Abdel-Latif SA, Hassib HB, Issa YM (2007) Spectrochim Acta A 67:950
52. Gomes JRB, Ribeiro da Silva MAV (2011) Curr Phys Chem 1:55 **(and references therein)**
53. Vladimirova KG, Freidzon AY, Kotova OV, Vaschenko AA, Lepnev LS, Bagaturyants AA, Vitukhnovskiy AG, Stepanov NF, Michael V, Alfimov MV (2009) Inorg Chem 48:11123
54. Li Y, Yang Z, Song B, Xia H, Wang Z (2017) Inorg Nano Met Chem 47:966

55. Zolezzi S, Decinti A, Spodine E (1999) Polyhedron 18:897
56. Zhang YL, Ruan WJ, Zhao XJ, Wang HG, Zhu ZA (2003) Polyhedron 22:1535
57. Bauernschmitt R, Ahlrichs R (1996) Chem Phys Lett 256:454
58. Shiau H-S, Liu W, Colby RH, Janik MJ (2013) J Chem Phys 139:204905
59. Zhou YH, Sun DL, Tao J, Chen LQ, Huang YF, Lia YK, Cheng Y (2014) J Coord Chem 67:2393
60. Zhou YH, Wan WQ, Sun DL, Tao J, Zhang L, Wei XW (2014) Z Anorg Allg Chem 640:249
61. Rajaei I, Mirsattari SN (2018) J Mol Struct 1163:36
62. Muthu S, Rajamani T, Karabacak M, Asiri AM (2014) Spectrochim Acta A 122:1
63. Politzer P, Murray JS (2002) Theor Chem Acc 108:134
64. Hannan A, Kang JY, Hong YK, Lee H (2013) Phytother Res 27:21
65. Mohibbullah M, Hannan MA, Choi JY, Bhuiyan MMH, Hong YK, Choi JS, Moon IS (2015) J Med Food 18:960
66. Hakanen J, Ruiz-Reig N, Tissir F (2019) Front Cell Neurosci 13:244
67. Dotti CG, Sullivan CA, Banker GA (1988) J Neurosci 8:1454
68. Fornasiero EF, Bonanomi D, Benfenati F, Valtorta F (2010) Cell Mol Life Sci 67:1383
69. Bullmore E, Sporns O (2012) Nat Rev Neurosci 13:336
70. Kaneko N, Sawamoto K (2009) Neurosci Res 63:155
71. Schmidt JR, Polik WF (2009) WebMO Enterprise, version .0; WebMO LLC: Holland, MI, USA; https://www.webmo.net
72. Frisch MJ, Trucks GW, Schlegel HB, Scuseria GE, Robb MA, Cheeseman JR, Scalmani G, Barone V, Petersson GA, Nakatsuji H, Li X, Caricato M, Marenich A, Bloino J, Janesko BG, Gomperts R, Mennucci B, Hratchian HP, Ortiz JV, Izmaylov AF, Sonnenberg JL, Williams-Young D, Ding F, Lipparini F, Egidi F, Goings J, Peng B, Petrone A, Henderson T, Ranasinghe D, Zakrzewski VG, Gao J, Rega N, Zheng G, Liang W, Hada M, Ehara M, Toyota K, Fukuda R, Hasegawa J, Ishida M, Nakajima T, Honda Y, Kitao O, Nakai H, Vreven T, Throssell K, Montgomery JA Jr, Peralta JE, Ogliaro F, Bearpark M, Heyd JJ, Brothers E, Kudin KN, Staroverov VN, Keith T, Kobayashi R, Normand J, Raghavachari K, Rendell A, Burant JC, Iyengar SS, Tomasi J, Cossi M, Millam JM, Klene M, Adamo C, Cammi R, Ochterski JW, Martin RL, Morokuma K, Farkas O, Foresman JB, Fox DJ (2016) Gaussian 09, Rev. D.01. Gaussian Inc, Wallingford
73. Lide DR (ed) (2008) CRC handbook of chemistry and physics, 89th edn. CRC Press, Boca Raton, p 9
74. Haynes WM (ed) (2011) CRC handbook of chemistry and physics, 92nd edn. CRC Press, Boca Raton, p 3.246
75. Nami SAA, Sarikavakli N, Alam MJ, Alam M, Park S, Ahmad S (2017) J Mol Struct 1138:90
76. Tomasi J, Mennucci B, Cammi R (2005) Chem Rev 105:2999
77. Dennington R, Keith T, Millam J (2009) Gauss view, Ver. 5. Semichem Inc., Shawnee Mission
78. Chemcraft - graphical software for visualization of quantum chemistry computations. https://www.chemcraftprog.com
79. Moon IS, Cho SJ, Jin I, Walikonis R (2007) Mol Cells 24:76